Electronic Supplementary Information (ESI) for Journal of Materials Chemistry C.
This journal is © The Royal Society of Chemistry 2024

Supporting Information

Understanding Phase Evolution of Ferroelectric $Hf_{0.5}Zr_{0.5}O_2$ Thin Films with Al_2O_3 and Y_2O_3 Inserted Layers †

Jonghoon Shin,[a] Haengha Seo,[a] Kun Hee Ye,[ab] Yoon Ho Jang,[a] Dae Seon Kwon,[a] Junil Lim,[a] Tae Kyun Kim,[a] Heewon Paik,[a] Haewon Song,[a] Ha Ni Kim,[a] Seung yong Byun,[a] Seong Jae Shin,[a] Kyung Do Kim,[a] Yong Bin Lee,[a] In Soo Lee,[a] Jung-Hae Choi,[b] and Cheol Seong Hwang*[a]

a Department of Materials Science and Engineering, and Inter-University Semiconductor Research Center, Seoul National University, Seoul, 08826, Republic of Korea. E-mail: cheolsh@snu.ac.kr

b Center for Electronic Materials, Korea Institute of Science and Technology, Seoul, 02792, Republic of Korea

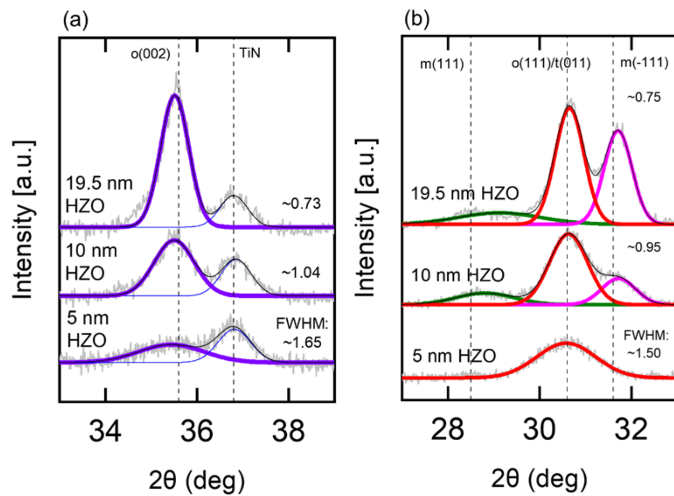

Fig. S1 Background subtracted GIXRD (incident angle: 0.5°) patterns (grey) of 5, 10, and 19.5 nm HZO for (a) o(002) (purple) and TiN (blue) peaks (b) overlapping o(111) and t(011) (red), m(111) (green) and m(-111) (pink) peaks, and the cumulative results for the mentioned peaks (black), respectively. To clearly show the changes in the Gaussian deconvoluted curves of o(002) (purple), m(111) (green), o(111)/t(011) (red), and m(-111) (pink) peaks, the GIXRD pattern was presented with two separate 2θ ranges of (a) 33° - 39° and (b) 27° - 33°.

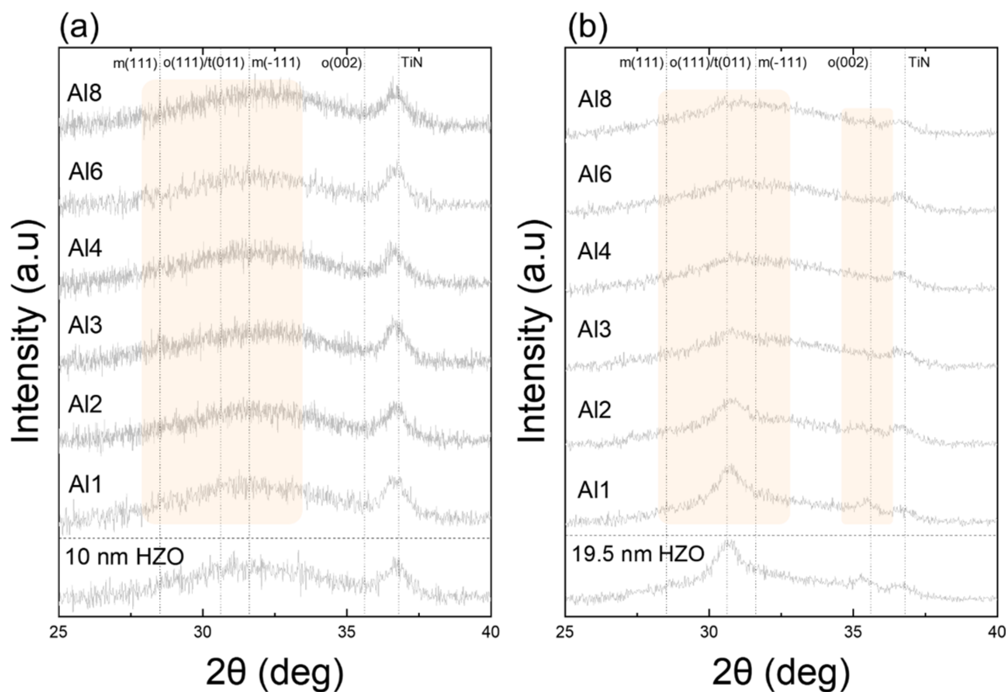

Fig. S2 GIXRD (incident angle: 0.5°) patterns of the as-deposited (a) 10 nm HZO and (b) 19.5 nm HZO with insertion of changing ALD cycles of Alp(10 nm) and Alp(19.5 nm) in the middle of films, respectively. The samples without any interlayer are also shown for comparison.

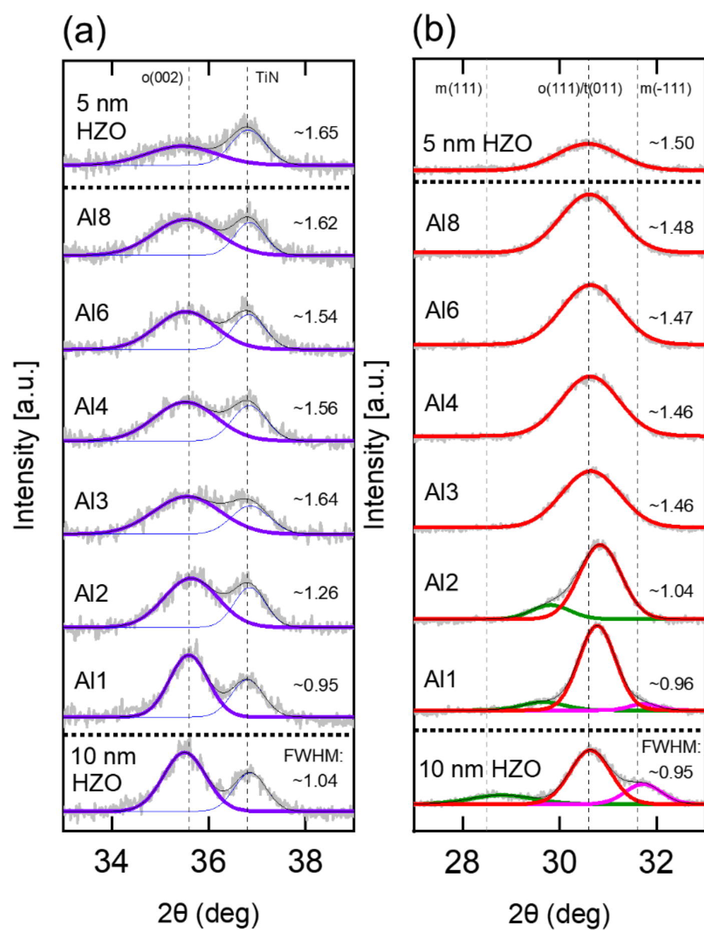

Fig. S3 Background subtracted GIXRD (incident angle: 0.5^{o}) patterns (grey) of Alp(10 nm) for (a) o(002) (purple) and TiN (blue) peaks (b) overlapping o(111) and t(011) (red), m(111) (green) and m(-111) (pink) peaks, and the cumulative results for the mentioned peaks (black), respectively. The 5 and 10 nm HZO are also added for comparison.

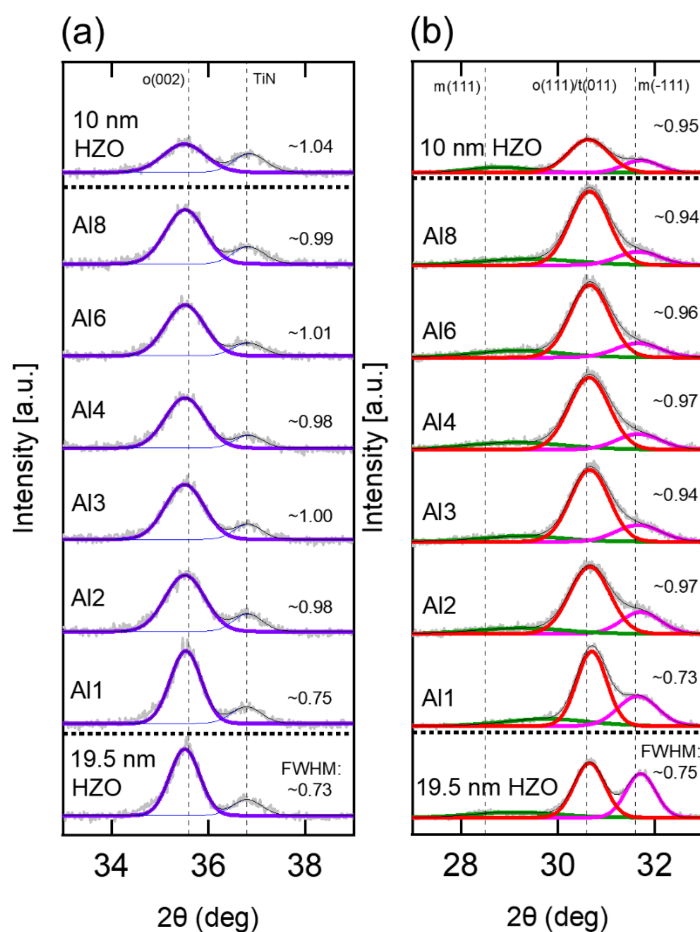

Fig. S4 Background subtracted GIXRD (incident angle: 0.5°) patterns (grey) of Alp(19.5 nm) for (a) o(002) (purple) and TiN (blue) peaks (b) overlapping o(111) and t(011) (red), m(111) (green) and m(-111) (pink) peaks, and the cumulative results for the mentioned peaks (black), respectively. The 10 and 19.5 nm HZO are also added for comparison.

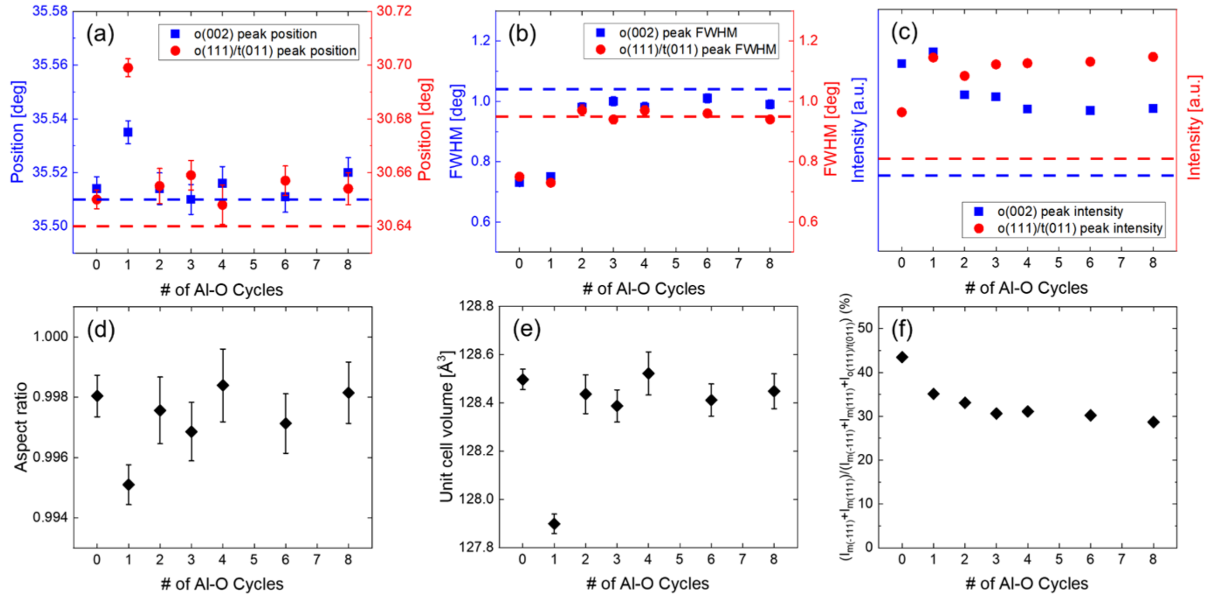

Fig. S5 The (a) peak positions, (b) FWHM, and (c) peak intensities of the o(002) and o(111)/t(011) peaks, and the (d) aspect ratio, (e) unit cell volume, and (f) m-phase areal ratio for the Alp(19.5 nm) films. The 10 nm HZO is also added for comparison with blue (o(002) peak) and red (o(111)/t(011) peak) dashed lines. Error bars are included for the peak positions and FWHM values from the standard deviation of the Gaussian fitting. Error bars of the aspect ratio and unit cell volume are estimated from the error of the peak positions of the o(002) and o(111)/t(011) peaks.

The Al1(19.5 nm) sample exhibited similar trends to the Al1, 2(10 nm) samples with diffused Al_2O_3 ILs, whereas the Al2, 3, 4, 6, and 8(19.5 nm) samples exhibited similar trends to the Al3, 4, 6, and 8(10 nm) samples with the divided HZO layers.

Fig. S5(a) shows the changes in the 2θ positions of the deconvoluted o(002) and o(111)/t(011) peaks for the Alp(19.5 nm) samples with changing Al_2O_3 IL cycles, respectively, where p=0 case corresponds to the 19.5 nm HZO film. In Fig. S5(a), the blue and red dashed lines indicate the positions of the 10 nm HZO film for the o(002) and o(111)/t(011) peaks, respectively. Both the o(002) and o(111)/t(011) peaks of the Al1(19.5 nm) exhibited a shift into the higher 2θ positions compared to the 19.5 nm HZO, attributed to the in-plane tensile stress from Al diffusion. However, the o(111)/t(011) peak displayed a significantly larger shift, which was attributed to the increased t(011)/(t(011)+o(111)) phase portion from the diffused

Al, also consistent with the thinner film cases. In contrast, those of the Al2, 3, 4, 6, and 8(10 nm) samples show a value similar to the 19.5 nm HZO (2θ ~ 35.51^{o} for o(002) and ~ 30.65^{o} for o(111)/t(011)), also consistent with the thinner film cases. Different from the thinner film cases, the o(002) and o(111)/t(011) peak positions of these samples did not display a noticeable shift into the higher 2θ positions compared to those of the undoped 10 nm HZO (within ~ 0.01-0.02) because the lower 10 nm HZO part of these films is not influenced by the growth strain effects at this thickness, as explained in the undoped HZO film section.

Fig. S5(b) shows the changes in the FWHM of the o(002) and o(111)/t(011) peaks for the Alp(19.5 nm) samples with changing Al_2O_3 IL cycles, respectively. The FWHM values of the o(002) and o(111)/t(011) peaks for the Al1(19.5 nm) were similar to those of the 19.5 nm HZO since the thinner Al_2O_3 did not interrupt the continuous grain growth. In contrast, FWHM values of the o(002) and o(111)/t(011) peaks for the Al2, 3, 4, 6, and 8(19.5 nm) are similar to those of the 10 nm HZO, aligning with the layer separation effect of the thick Al_2O_3.

Fig. S5(c) shows the changes in the peak intensities of the o(002) and o(111)/t(011) peaks for the Alp(19.5 nm) samples with changing Al_2O_3 IL cycles, respectively. The o(002) and o(111)/t(011) peak intensities of the Al2, 3, 4, 6, and 8(19.5 nm) were approximately twice that of the 10 nm HZO, confirming the presence of two divided ~ 10 nm HZO parts. The o(002) peak intensity of the Al1(19.5 nm) sample is comparable to that of the 19.5 nm HZO, also consistent with the thinner film cases.

Fig. S5(d) and (e) show the changes in the AR and unit cell volume of the Alp(19.5 nm) samples with changing Al_2O_3 IL cycles, respectively. The AR and unit cell volume of the Al1(19.5 nm) was lower than the 19.5 nm HZO, confirming the enhanced t/(o+t) phase portion with the Al diffusion, aligning with the peak position observations. Different from the thinner films, however, the AR and unit cell volume of Al1(19.5 nm) decreased compared to the 19.5

nm HZO by ~ 0.3% and ~ 0.5%, respectively, displaying smaller decreases compared to the Al1, 2(10 nm) cases. This difference suggested that the phase change effects of the diffused Al were more pronounced in the thinner films. The AR and unit cell volume values of the Al2, 3, 4, 6, and 8(19.5 nm) samples showed minimal changes compared to the 10 nm HZO since the division of the HZO films did not significantly affect the relative portion changes between the o- and t-phases as the diffused Al cases.

Fig. S5(f) shows the relative m-phase fraction changes for the Alp(19.5 nm) samples with changing Al_2O_3 IL cycles. The Al1(19.5 nm) exhibited a m-phase areal fraction of ~ 35%, lower than that of the 19.5 nm HZO (~ 44%). The peak positions, AR, and unit cell volume changes of the Al1(19.5 nm) showed the increased t/(o+t) phase portion with Al diffusion. Hence, the diffused Al reduced the m-phase and enhanced the formation of the t-phase, consistent with the thinner film cases. The Al2, 3, 4, 6, and 8(19.5 nm) samples showed retained m-phases with a peak areal fraction of ~ 29-33%. This m-phase areal fraction was similar to the 10 nm HZO (~ 34%), as the films were separated into two ~ 10 nm-thick HZO layers.

It was notable that the Al2(19.5 nm) sample already belonged to the group of samples with continuous Al_2O_3, suggesting that the two cycles of IL between the thicker HZO (~ 10 nm) had a lower tendency toward diffusion than the case with thinner HZO layers (~ 5 nm). The higher crystalline quality of the 10 nm HZO film than the 5 nm HZO film appears to suppress the Al diffusion, but identifying precise reasons for such behavior needs further study.

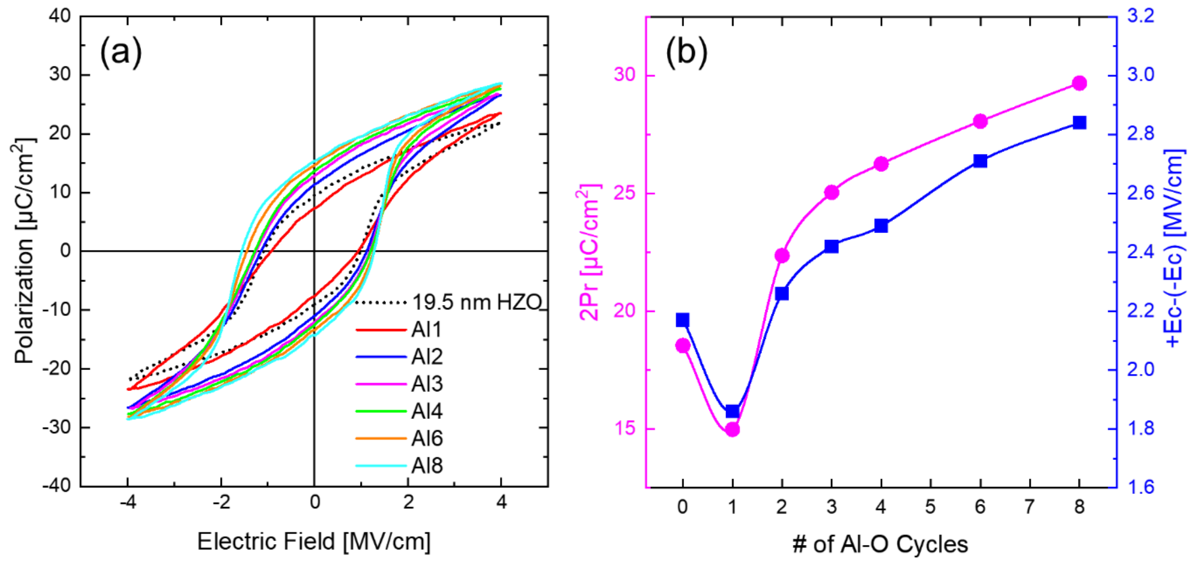

Fig. S6 (a) Polarization-electric field (P-E) curves and the (b) changes in the $2P_r$ and $+E_c$-($-E_c$) values of the 19.5 nm $Hf_{0.5}Zr_{0.5}O_2$ with insertion of changing ALD cycles of Alp(19.5 nm) in the middle of films.

Fig. S6(a) shows the P-E curves of the Alp(19.5 nm) samples in the pristine state (dotted curve for the 19.5 nm HZO for comparison), and Fig. S6(b) shows the $2P_r$ and the $+E_c$-($-E_c$) changes of the P-E curves displayed in Fig. S6(a). The P-E curve of the Al1(19.5 nm) exhibited lower $2P_r$ and $+E_c$-($-E_c$) values compared to the 19.5 nm HZO, despite the significant reduction in the m-phase observed in Fig. S5(f). These findings confirmed that the diffused Al reduced the m-phase and enhanced the t-phase. In contrast, the Al2, 3, 4, 6, and 8(19.5 nm) samples displayed increased $2P_r$ values. This behavior is again due to the layer separation effect, increasing the films' o/(m+o+t) phase portion. The $2P_r$ values increased with higher p, suggesting a more effective m-phase reduction and enhanced o-phase formation. The $+E_c$-($-E_c$) values of these samples also exhibited an increasing trend with increasing p because the continuous Al_2O_3 ILs acted as a series resistor during FE switching with higher tunneling resistance at higher thickness.[1, 2]

Notably, the impact of diffused Al_2O_3 on the changes in electrical characteristics was less pronounced when inserted in the center of 19.5 nm HZO compared to 10 nm HZO. The $2P_r$

and $+E_c$-($-E_c$) values of Al1, 2(10 nm) samples in Fig. 4(b) exhibited significant reductions of ~ 13.4 - 14.6 μC cm^{-2} and ~ 0.45 - 0.5 MV cm^{-1}, respectively, compared to 10 nm HZO. However, the Al1(19.5 nm) sample in Fig. S6(b) displayed much smaller reductions of ~ 3.6 μC cm^{-2} and ~ 0.3 MV cm^{-1} compared to 19.5 nm HZO.

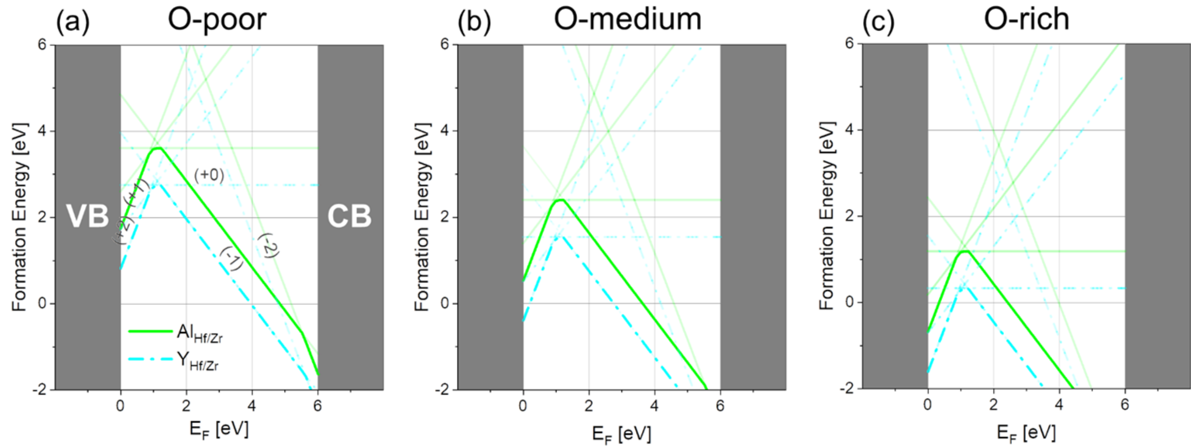

Fig. S7 The formation energy of substitutional Al ($Al_{Hf/Zr}$, light green) and Y ($Y_{Hf/Zr}$, sky blue) in $Hf_{0.5}Zr_{0.5}O_2$ under (a) "O-poor" ($\Delta\mu_O$ = -4.84 eV), (b) "O-medium" ($\Delta\mu_O$ = -2.42 eV), and (c) "O-rich" ($\Delta\mu_O$ = 0 eV) conditions. The defect formation energy was calculated by linear interpolation between HfO_2 and ZrO_2. The dark gray regions represent the valence band (VB) and conduction band (CB), and the white regions represent the bandgap of tetragonal $Hf_{0.5}Zr_{0.5}O_2$. The formation energies were calculated by density functional theory using the generalized gradient approximation of Perdew-Burke-Ernzerhof (GGA-PBE) exchange-correlation functional. The "O-poor" condition corresponds to pure metal cases and is irrelevant to the experimental context. The "O-medium" and "O-rich" conditions correspond to cases involving higher and lower Al/Y IL ALD cycles, respectively, relevant to the experiments conducted. $Y_{Hf/Zr}$ exhibited negative formation energy near the bandgap center under both the "O-medium" and "O-rich" conditions, indicating that substituting $Hf^{4+}$and Zr^{4+} sites in $Hf_{0.5}Zr_{0.5}O_2$ with Y^{3+} ions is energetically favorable regardless of the number of Y ALD cycles. In contrast, $Al_{Hf/Zr}$ exhibited negative formation energy near the bandgap center only under the "O-rich" condition while exhibiting positive formation energy under the "O-medium" condition. These results indicated that substituting $Hf^{4+}$and Zr^{4+} sites in $Hf_{0.5}Zr_{0.5}O_2$ with Al^{3+} ions is concentration-dependent and that the Al IL can only diffuse into the $Hf_{0.5}Zr_{0.5}O_2$ for lower Al ALD cycles. The calculation method is identical to our previous study,

of which details and further analyses can be found elsewhere.[3]

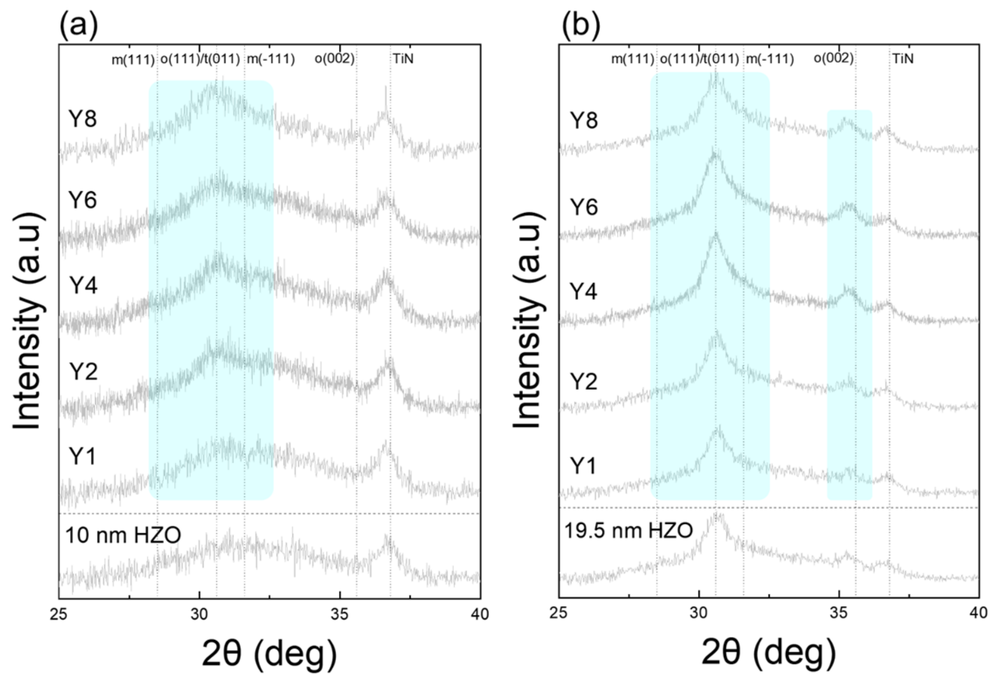

Fig. S8 GIXRD (incident angle: 0.5^{o}) patterns of the as-deposited (a) 10 nm HZO and (b) 19.5 nm HZO with insertion of changing ALD cycles of Yp(10 nm) and Yp(19.5 nm) in the middle of films, respectively. The samples without any interlayer are also shown for comparison.

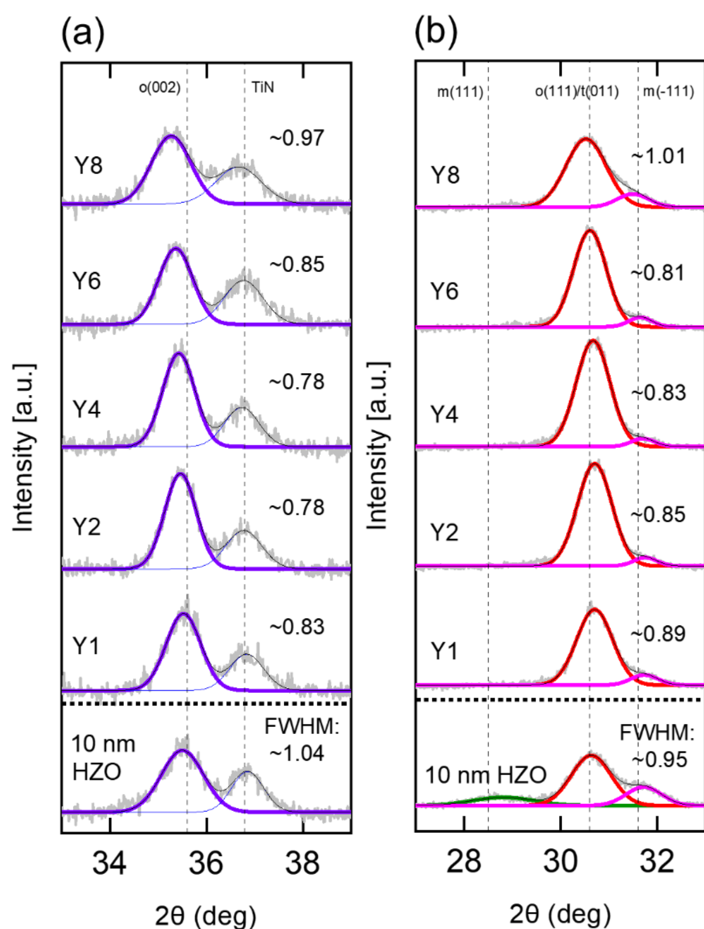

Fig. S9 Background subtracted GIXRD (incident angle: 0.5°) patterns (grey) of Yp(10 nm) for (a) o(002) (purple) and TiN (blue) peaks (b) overlapping o(111) and t(011) (red), m(111) (green) and m(-111) (pink) peaks, and the cumulative results for the mentioned peaks (black), respectively. The 10 nm HZO is also added for comparison.

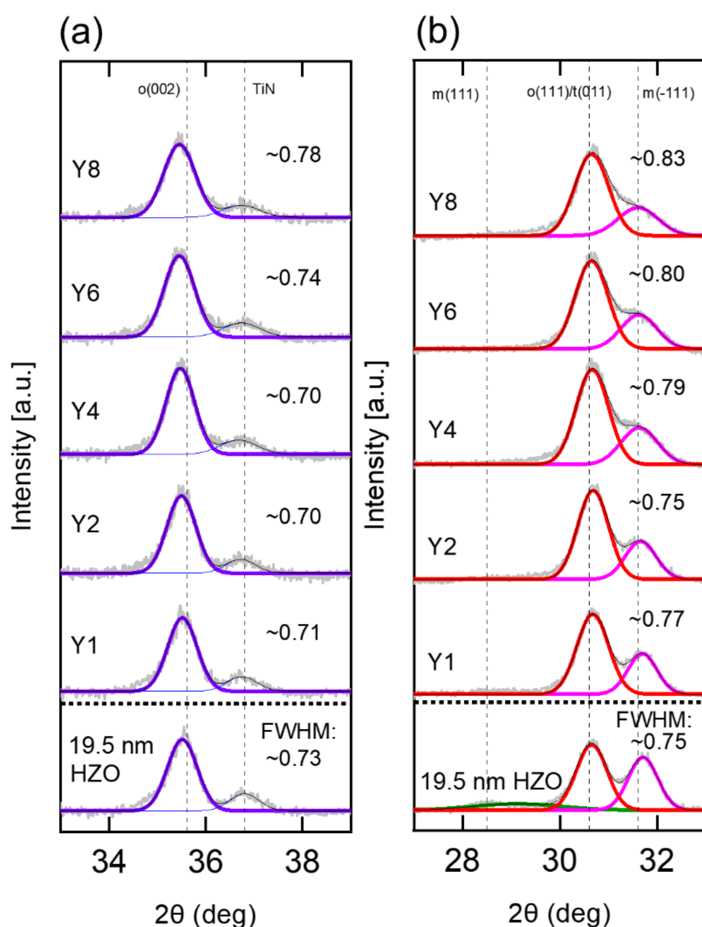

Fig. S10 Background subtracted GIXRD (incident angle: 0.5^{o}) patterns (grey) of Yp(19.5 nm) for (a) o(002) (purple) and TiN (blue) peaks (b) overlapping o(111) and t(011) (red), m(111) (green) and m(-111) (pink) peaks, and the cumulative results for the mentioned peaks (black), respectively. The 19.5 nm HZO is also added for comparison.

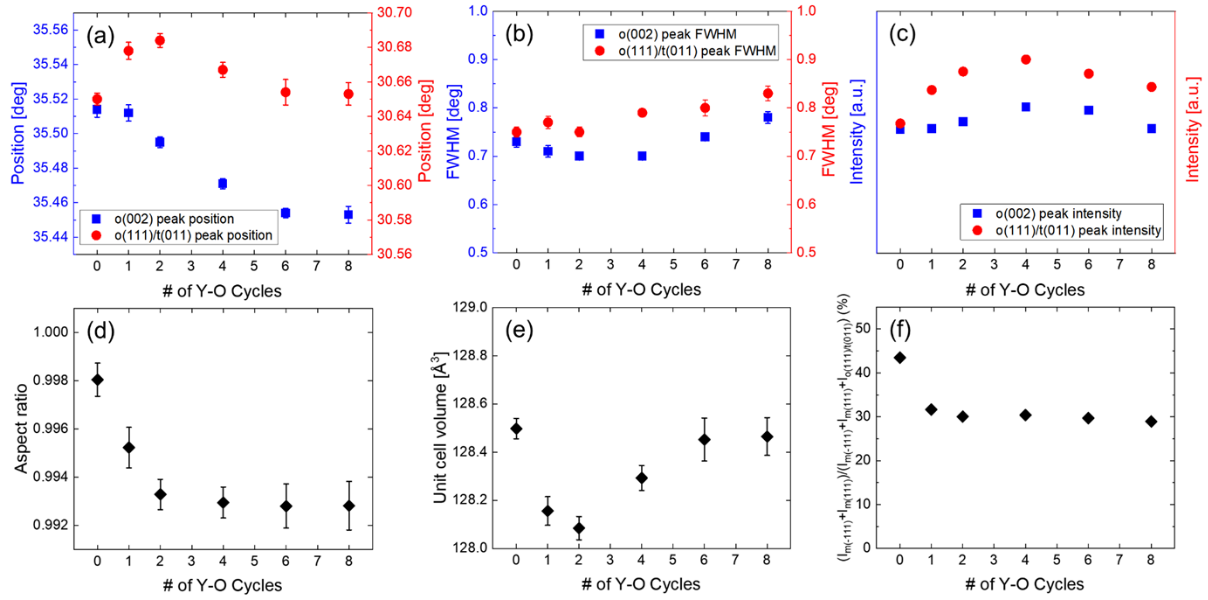

Fig. S11 The (a) peak positions, (b) FWHM, and (c) peak intensities of the o(002) and o(111)/t(011) peaks, and the (d) aspect ratio, (e) unit cell volume, and (f) m-phase areal ratio for the Yp(19.5 nm) films. Error bars are included for the peak positions and FWHM values from the standard deviation of the Gaussian fitting. Error bars of the aspect ratio and unit cell volume are estimated from the error of the peak positions of the o(002) and o(111)/t(011) peaks.

The o(002) peak positions shifted monotonically towards lower positions due to the in-plane compress stress induced by the diffused Y. In contrast, the o(111)/t(011) peak positions were affected by both the strain from Y diffusion (decreasing the peak position) and the increased t(011)/(t(011)+o(111)) phase portion (increasing the peak position). The intensities of both the o(002) and o(111)/t(011) peaks increased for Y1, 2, and 4(19.5 nm) due to enhanced grain growth, while those of the Y6, 8(19.5 nm) decreased due to the development into a mosaic structure. The AR values decreased with increasing p at lower p and saturated at higher p due to the limited impact of diffused Y_2O_3 on the phase fractions changes within the nearby regions of the HZO. The unit cell volume decreased up to p = 2 due to the dominant t-phase enhancement effect and increased for Y4, 6, and 8(19.5 nm) due to the dominant larger Y^{3+} radius effect.

However, there are differences, too. Different from the thinner film cases, the FWHM of the

o(002) (~ 0.70-0.78) and o(111)/t(011) (~ 0.75-0.83) peaks did not exhibit significant differences with changing p. The changes in positions and intensities of the o(002) and o(111)/t(011) peaks from Y diffusion, although displaying similar tendencies to the thinner film cases, were considerably less pronounced compared to the changes shown for the Yp(10 nm) films. Moreover, the reduction in m-phase areal fraction by Y diffusion in the thicker films in Fig. S11(f) (~ 12-16% reduction) showed smaller decreases compared to the thinner films in Fig. 7(f) (~ 22-29% reduction). Furthermore, the decrease in AR by Y diffusion in the thicker films in Fig. S11(d) (~ 0.3-0.5%) showed smaller decreases compared to the thinner films in Fig. 7(d) (~ 0.5-1%). These findings suggested that Y doping exhibited consistent effects in 10 nm and 19.5 nm HZO films, but its impact was more significant in the thinner films.

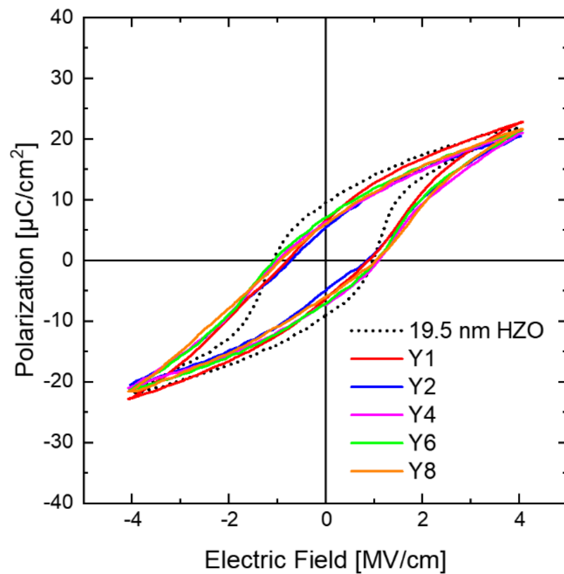

Fig. S12. P-E curves of the 19.5 nm HZO with insertion of changing ALD cycles of Yp(19.5 nm) in the middle of films.

Fig. S12 shows the P-E curves of the Yp(19.5 nm) samples in the pristine state (dotted curve for the 19.5 nm HZO for comparison). The P-E curves exhibited similar reductions in $2P_r$ values compared to the 19.5 nm HZO, confirming that the Y diffusion suppressed the m-phase formation and enhanced the t-phase. Notably, the influence of diffused Y_2O_3 on the electrical

characteristics was more pronounced in the case of the 10 nm HZO compared to the 19.5 nm HZO. The P-E curves of the Yp(10 nm) samples in Fig. 9 exhibited significant reductions in $2P_r$ values compared to 10 nm HZO. In contrast, the Yp(19.5 nm) samples in Fig. S12 displayed much smaller reductions.

References

[1] A. Q. Jiang, H. J. Lee, G. H. Kim and C. S. Hwang, *Adv. Mater.* 2009, **21**, 2870-2875.

[2] H. J. Kim, M. H. Park, Y. J. Kim, Y. H. Lee, W. Jeon, T. Gwon, T. Moon, K. D. Kim and C. S. Hwang, *Appl. Phys. Lett.* 2014, **105**.

[3] H. Seo, I. W. Yeu, D. S. Kwon, D. G. Kim, J. Lim, T. K. Kim, H. Paik, J. H. Choi and C. S. Hwang, *Adv. Electron. Mater.* 2022, **8**, 2200099.